Kubo *et al.*
*Progress in Earth and Planetary Science* (2022) 9:21
https://doi.org/10.1186/s40645-022-00480-9

Progress in Earth and Planetary Science

RESEARCH ARTICLE Open Access

# Back-transformation processes in high-pressure minerals: implications for planetary collisions and diamond transportation from the deep Earth

Tomoaki Kubo[1*], Ko Kamura[2], Masahiro Imamura[2], Yoshinori Tange[3], Yuji Higo[3] and Masaaki Miyahara[4]

**Abstract**

We conducted back-transformation experiments in ringwoodite, bridgmanite, and lingunite at 0.47–8.1 GPa and 310–920 °C by in situ X-ray observation method. Ringwoodite back-transformed to olivine by grain-boundary nucleation and growth mechanism. The site saturation occurred at the early stage under the conditions far from the equilibrium boundary, and we observed the growth-controlled back-transformation kinetics in ringwoodite. The growth kinetics determined in the present study is largely different from that in the previous study (Reynard et al. in Am Min 81:585–594, 1996), which may be due to the effects of water. Bridgmanite did not directly back-transform to the stable phase orthoenstatite at ~ 1–4 GPa, but first becomes amorphous with increasing temperatures. We observed kinetics of the orthoenstatite crystallization from amorphous bridgmanite that was controlled by both nucleation and growth processes. The temperature range in the amorphous state became narrow with increasing pressures, and the direct back-transformation to high-P clinoenstatite without amorphization eventually occurred at 8 GPa. Amorphization was also observed in lingunite when increasing temperature at ~ 1.5 GPa; however, the plagioclase crystallization proceeded before the complete amorphization. The back-transformation in ringwoodite variedly occurs in shocked meteorites depending on the degree of the post-shock annealing, which can be reasonably interpreted based on the growth kinetics. On the other hand, the presence of hydrous ringwoodite in diamond inclusions cannot be explained without the help of residual stress. The present study also indicates that complete amorphization or the back-transformation to enstatite is unavoidable in bridgmanite during the post-shock annealing. This is inconsistent with the presence of crystalline bridgmanite in shocked meteorites, still requiring further investigations of kinetic behaviors in shorter timescales.

**Keywords:** High-pressure mineral, Shocked meteorite, Diamond inclusion, Back-transformation, Synchrotron radiation, High-pressure experiment, Transformation kinetics, Amorphization

## 1 Introduction

High-pressure minerals stable at deep mantle pressures have been naturally found on Earth such as in shocked meteorites and diamond inclusions, which provides important constraints on detailed processes of planetary collisions and deep mantle dynamics. Because the timescales are limited in these dynamic processes, the reactions often remain incomplete and/or metastable state. The back-transformation also occurs during the transportation to the surface of the Earth, which complicates the interpretation. Therefore, considering the reaction kinetics is potentially important to deduce the P–T–t history of these dynamic processes.

*Correspondence: kubotomo@geo.kyushu-u.ac.jp
[1] Department of Earth and Planetary Sciences, Faculty of Sciences, Kyushu University, Fukuoka 819-0395, Japan
Full list of author information is available at the end of the article

In shocked meteorites, experimentally determined kinetics on the forward (prograde) reactions have been widely used to investigate shock history including shock duration and size of the impactor (e.g., Ohtani et al. 2004; Xie and Sharp 2007; Kubo et al. 2010, 2015; Miyahara et al. 2010). The forward kinetics have also been discussed to understand dynamics of subducting oceanic plates (e.g., Rubie and Ross 1994; Kubo et al. 2009).

On the other hand, the importance of the backward (retrograde) reactions for the dynamic processes has not been extensively focused. There have been some reports on the back-transformation of high-pressure phases such as ringwoodite, majoritic garnet, and lingunite originally produced in or near shock melt veins of a chondrite during atmospheric entry (Kimura et al. 2004; Fukimoto et al. 2020). They observed back-transformation texture gradually changed with the distance from the fusion crust, and proposed the mechanisms of the back-transformation. In addition to the atmospheric passage event, the post-shock annealing can also cause the back-transformation (e.g., Walton 2013). Hu and Sharp (2017) have discussed post-shock thermal history on the basis of the textural observations combined with thermal models of shock melt cooling and reaction kinetics. They proposed strong shock events can erase high-pressure signatures by the complete back-transformation in post-shock annealing.

Survival of high-pressure minerals in diamond inclusions is thought to be more difficult because of the longer timescales for the diamond transportation. The low-pressure polymorphs with having distinct chemical compositions and phase assemblages are often used as the evidence for the presence of the former high-pressure phases such as bridgmanite (e.g., Hayman et al. 2005). Majoritic garnet have been commonly found in diamond avoiding the back-transformation (Moore and Gurney 1985; Tappert et al. 2005) probably due to the slow kinetics of the decompositional back-transformation (Nishi et al. 2010). Recent new findings of ringwoodite (Pearson et al. 2014) and davemaoite (Tschauner et al. 2021) in diamond are enigmatic because the polymorphic back-transformation rate is thought to be faster, in which the residual stress in the host diamond may be important for the preservation of high-pressure phases.

In spite of the important information from survival of high-pressure phases in shocked meteorites and diamond inclusions, experimental data on mechanisms and kinetics of the back-transformation have not been investigated adequately so far. Most previous data were obtained at ambient pressure, and the pressure and temperature dependences on the kinetics have been poorly known. Here we report experimental results on the polymorphic back-transformation in ringwoodite, bridgmanite, and lingunite at high pressures and temperatures. In situ X-ray observations with synchrotron radiation enable us to catch the detailed reaction processes and kinetics. Based on the results obtained, we briefly discussed survival of high-pressure minerals in shocked meteorites and diamond inclusions.

## 2 Experimental procedure

We used three kinds of starting materials, polycrystalline ringwoodite, bridgmanite, and lingunite, for the back-transformation experiments. These high-pressure minerals were synthesized using a KAWAI-type multi-anvil (MA) apparatus (QDES) at Kyushu University, from San Carlos olivine single crystal, San Carlos orthopyroxene ($En_{89.4}Fs_{8.6}Wo_{2.0}$) powder, and natural oligoclase ($Ab_{72.6}An_{23.0}Or_{4.4}$) powder, respectively. The sample assembly was the same as that used in the previous study (Kubo et al. 2017). The synthesis conditions for ringwoodite and bridgmanite were 22 GPa, 1400 °C for 180 min, and 25 GPa, 1800 °C for 60 min, respectively. Lingunite was synthesized as a metastable phase at 20 GPa, 1160 °C for 5 min heating (Kubo et al. 2017). The synthesized polycrystalline high-pressure phases were cut into the disks with ~ 800–1000 μm in diameter and ~ 350–750 μm in height, and used as the starting material for the back-transformation experiments. Unpolarized infrared absorption spectra of the synthesized ringwoodite were obtained in air using Fourier-transform infrared spectrometer. The broad absorption peak was observed at ~ 3400 $cm^{-1}$. The water content was estimated to be ~ 1400 wt. ppm $H_2O$ by integrating the broad absorption band based on the calibration by Paterson (1982). The observed absorption spectra are almost consistent with those for ringwoodite containing similar amounts of water (Kawazoe et al. 2016). A small amount of stishovite were contained in the bridgmanite sample. Majorite was also confirmed in one of the starting materials of bridgmanite (Run M2715).

We performed the back-transformation experiments by in situ X-ray observations at the synchrotron radiation facilities of the Photon Factory (AR-NE5C) and SPring-8 (BL04B1) using the DIA-type apparatuses MAX-80 and SPEED1500 Mk-II, respectively. A MA6-6-type assembly was used to generate pressures (Nishiyama et al. 2008). The truncated edge length (TEL) of the second-stage anvils is 4 or 6 mm. The sample assembly was composed of boron-epoxy pressure medium, a cylindrical graphite heater, a Cu electrode, and a hBN sample capsule (Fig. 1a). Temperature was measured at the center of the sample assembly with W3%Re–W25%Re thermocouples. The temperature fluctuation during heating was less than ± 5 °C. We put a mixture of NaCl and hBN powders into the hBN capsule, and then the disk-shaped starting material was embedded in the powder mixture. In some

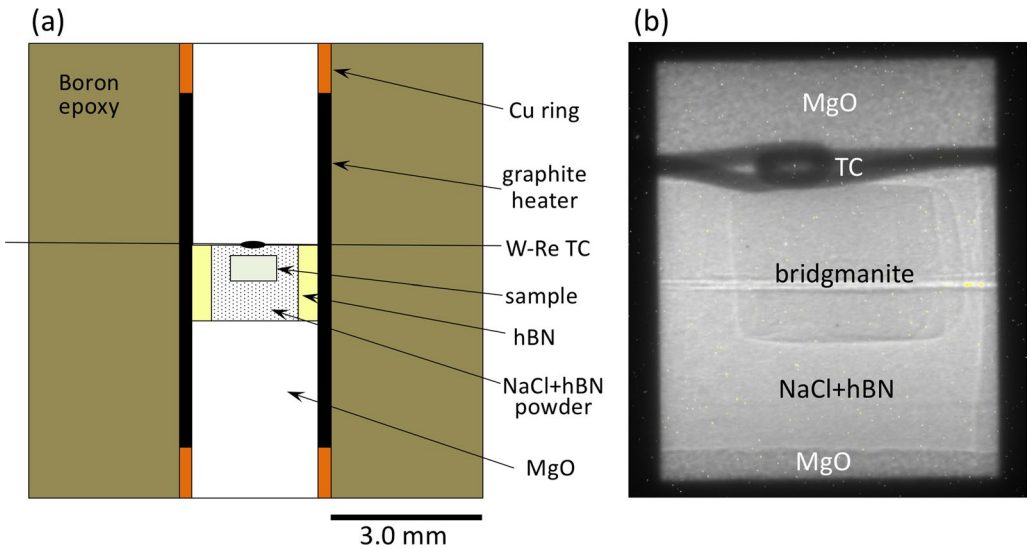


**Fig. 1** Sample assembly used in the back-transformation experiments (TEL6 system). **a** Cross section of the sample assembly. **b** Its radiography image around the sample at a load of 5 ton (Run M2621)

experiments, we put two kinds of starting materials in a capsule above and below the thermocouples. For the run at the lowest pressure of ~ 0.5 GPa (Run M2932), only hBN powder was used to avoid melting of NaCl.

White X-rays from synchrotron radiation were used as the incident X-ray beam in most of runs. We monitored thermocouples and samples in a capsule by radiography image to locate the position for the measurement of X-ray diffraction (XRD) pattern (Fig. 1b). The diffracted beam was measured in the vertical or horizontal direction between the second-stage anvils by the energy-dispersive method using a Ge solid-state detector. The glancing angle ($2\theta$) of the solid-state detector was fixed at 5.0°. A conical slotted anvil was used at the downstream side to measure XRD patterns in the horizontal direction. The sample was first compressed at room temperature and then heated in 100–300 K steps at ~ 3.3–8.3 °C/s with a constant load. The temperature was held constant at each step during the collection of diffraction patterns every 10 to 500 s.

In one experiment for ringwoodite (Run M2096), monochromatic X-ray of 50 keV was used as an incident X-ray beam and two-dimensional X-ray diffraction (2D-XRD) patterns were measured by CCD detector. The obtained 2D-XRD pattern was converted to 1D-XRD pattern to analyze kinetic data in the same way as in other runs. The sample assembly was almost the same as that shown in Fig. 1 except that the starting ringwoodite was directly put into the MgO capsule instead of the hBN capsule without using the NaCl + hBN powder, and sandwiched between two $Al_2O_3$ rods instead of MgO rods. Temperature was measured at the bottom of the sample by the thermocouples. Although the different experimental method was applied in this run, we analyzed the kinetic data together with all runs as the quality of the data was similar.

The pressure was calculated from the unit-cell volume of NaCl (Brown 1999) in most of runs. For the runs without using NaCl powder for sample medium, the unit-cell volume of ringwoodite was used for the pressure calculation (Nishihara et al. 2004). The pressure uncertainties are estimated to be less than ± 0.1 GPa in most of runs from the errors of the volume calculation. Reaction microstructures in some recovered samples were investigated using a field emission scanning electron microscope (FE-SEM, JEOL JSM-70001F) with an electron back-scattered diffraction (EBSD) system.

## 3 Results and discussion

### 3.1 In situ X-ray and SEM observations of the back-transformation processes

Eight experiments were conducted using ringwoodite at 0.47–7.5 GPa and 455–920 °C. We observed the back-transformation of ringwoodite to olivine at higher temperature than 650–700 °C as summarized in Fig. 2 and Table 1. The back-transformation temperatures slightly increase with pressures. Figure 3 shows an example of changes of XRD patterns from ringwoodite to olivine at 4.1 GPa and 820 °C. We did not observe formation of metastable phase and amorphization during the back-transformation of ringwoodite in our experimental conditions.

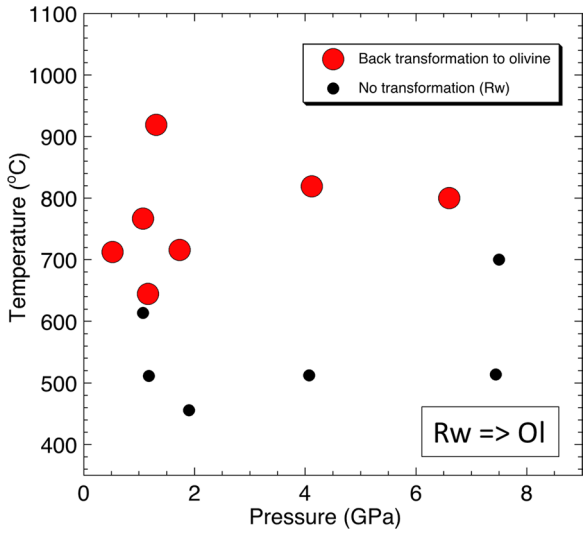


**Fig. 2** P–T conditions for the back-transformation in ringwoodite. The back-transformation to olivine occurred at higher than ~600–700 °C (red circles)

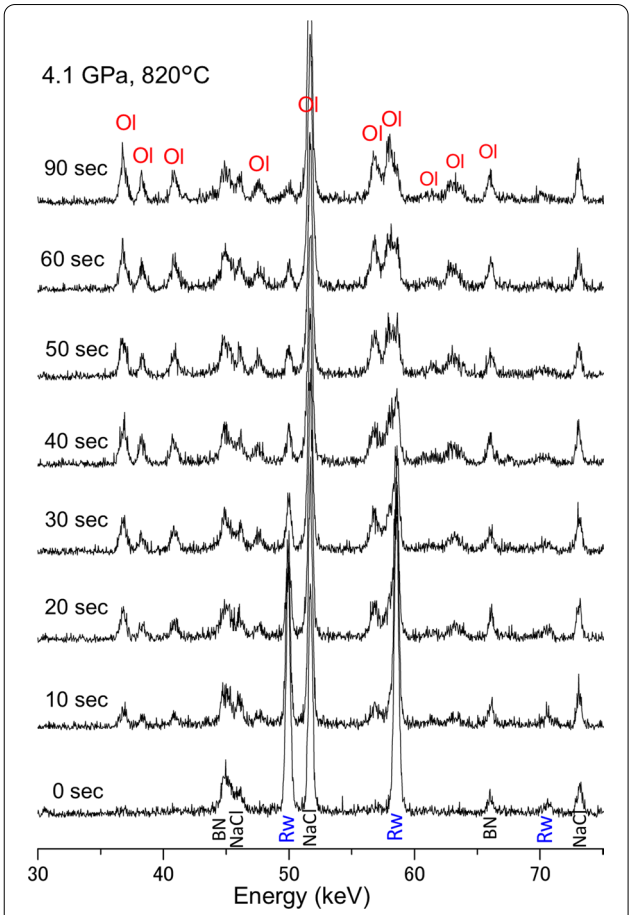


**Fig. 3** Changes of XRD patterns during the back-transformation in ringwoodite. Ringwoodite (Rw) directly transforms to olivine (Ol) at 4.1 GPa and 820 °C (Run M2620)

Polycrystalline microstructure of the starting material is shown in Fig. 4a. The starting ringwoodite exhibits equiangular texture, and the grain size was estimated to be 8.9 μm by intercept method from several SEM images. Figure 4b shows the reaction microstructure of the partially back-transformed sample at 1.2 GPa and 645 °C (Run M2893). In this image, the darker regions are present between the brighter grains with several microns in size. The EBSD analysis indicates that the brighter grains are ringwoodite. The final transformed fraction and the growth distance of olivine

**Table 1** P–T–t conditions and estimated values of kinetic parameters for the back-transformation from ringwoodite to olivine

| Run No. | Pressure (GPa) | Temperature (°C) | Duration (s) | Δ*Gr* (J/mol) | *n* | ln *k* | Growth rate[1] (m/s) |
|---|---|---|---|---|---|---|---|
| M2932 | 0.5 | 715 | 360 | −45,101 | 0.67 | −4.36 | $3.0\ (0.1) \times 10^{-9}$ |
| M2716 | 1.1 | 615 | 1620 | −41,382 | No transformation | | |
| | 1.1 | 765 | 1225 | −43,039 | 0.64 | −1.96 | $5.7\ (0.4) \times 10^{-8}$ |
| M2893 | 1.2 | 510 | 1055 | −39,817 | No transformation | | |
| | 1.2 | 645 | 18,340 | −41,283 | 0.85 | −9.10 | $3.8\ (0.1) \times 10^{-11}$ |
| M2614 | 1.3 | 920 | 135 | −43,924 | Completed within 10 s | | |
| M2714 | 1.9 | 455 | 3920 | −36,326 | No transformation | | |
| | 1.7 | 715 | 2720 | −39,917 | 0.89 | −6.74 | $7.2\ (0.1) \times 10^{-10}$ |
| M2620 | 4.1 | 510 | 445 | −28,161 | No transformation | | |
| | 4.1 | 820 | 230 | −31,202 | 1.11 | −3.50 | $5.8\ (0.4) \times 10^{-8}$ |
| M2717 | 7.4 | 515 | 435 | −16,122 | No transformation | | |
| M2096 | 7.5 | 700 | 415 | −17,412 | No transformation | | |
| | 6.6 | 800 | 2590 | −21,536 | 0.91 | −5.63 | $2.9\ (0.2) \times 10^{-9}$ |

[1] The uncertainties in growth rate are listed in parentheses

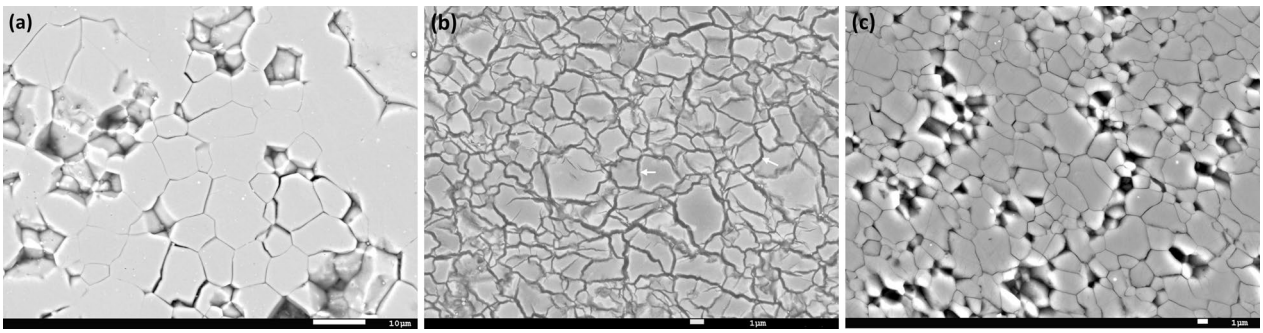


**Fig. 4** Back-scattered electron (BSE) images showing back-transformation microstructures in ringwoodite. **a** Polycrystalline microstructure of the starting material (ringwoodite). **b** Fine-grained olivine (darker regions indicated by white arrows) forms reaction rims along grain boundaries of parental ringwoodite grains in the partially back-transformed sample recovered at 1.2 GPa and 645 °C (Run M2893). **c** Polycrystalline olivine after the completion of the back-transformation at 6.6 GPa and 800 °C (Run M2096)

are estimated to be ~ 34 vol% and ~ 0.7 μm, respectively, from analysis of kinetic data in this run. These observations suggest that the darker region between the brighter ringwoodite grains consists of newly transformed fine-grained olivine although the phase identification by EBSD was difficult due to the small grain size. We do not have any evidences for intra-crystalline nucleation such as lamellar texture, and therefore the back-transformation of ringwoodite proceeds by grain-boundary nucleation and growth. This is consistent with that observed in shocked meteorites (Fukimoto et al. 2020). The olivine texture after the completion of the back-transformation at higher temperature of 800 °C and 6.6 GPa (Run M2096) is shown in Fig. 4c. The grain size becomes much larger (a few microns), which may result from the grain growth following the back-transformation.

We conducted eight experiments on bridgmanite at 1.1–8.1 GPa and 310–920 °C (Fig. 5 and Table 2). At ~ 1 GPa, we observed disappearance of diffraction peaks in bridgmanite and increase in halo pattern with temperatures from 310 to 615 °C (Fig. 6a), suggesting that the thermal-induced amorphization occurred in bridgmanite. The amorphization quickly progressed when increasing temperature, but hardly with time when keeping the temperature constant. As a result, diffraction peaks in bridgmanite were still present and the sample was in the partially amorphous state in the temperature range 410–510 °C. The complete amorphization was observed at 615–715 °C, and then crystallization of orthoenstatite occurs with disappearance of the halo pattern at 770 °C (Fig. 6b). These results are summarized in Fig. 5 and Table 2.

The amorphization temperature increases with pressures. At ~ 4 GPa, the bridgmanite amorphization did not start until the temperature reached 720 °C. It completed at 820 °C in 30 s, followed by the orthoenstatite crystallization (Fig. 6c). These observations indicate that bridgmanite does not directly back-transform to the stable phase orthoenstatite at ~ 1–4 GPa, but first becomes amorphous with increasing temperatures. The temperature range in the amorphous state becomes narrow with increasing pressures because the pressure dependence of the amorphization temperature is much greater than that of the crystallization temperature (Fig. 5). The amorphous state eventually vanishes at ~ 8 GPa, and bridgmanite directly back-transforms to high-P clinoenstatite at 820 °C without amorphization (Fig. 6d). Thus, the amorphization behavior in bridgmanite largely changes with pressures. Microstructures in the amorphized bridgmanite and crystallized orthoenstatite were not clear in the FE-SEM images. Figure 7 shows microstructures of partially back-transformed bridgmanite to high-P clinoenstatite at 7.9 GPa and 820 °C (Run M2715). High-P clinoenstatite is expected to further transform to low-P clinoenstatite during decompression to ambient pressure (Angel et al. 1992; Akashi et al 2009). We infer that the brighter phase is the relict bridgmanite and the darker phase is the low-pressure phase in this image. The grain size of parental bridgmanite is not clear but roughly estimated to be ~ 10–20 μm. Figure 7 suggests that the back-transformation proceeds by both inter- and intra-crystalline processes, resulting in a crazing texture of relict bridgmanite. The back-transformation may also occur in cracks that might be produced in bridgmanite grains when decompression and recompression stages at room temperature. Further investigations of these samples using TEM will be required for understanding the detailed process of amorphization and crystallization.

We conducted one experiments on lingunite at ~ 1.5–1.8 GPa and up to 820 °C (Fig. 8). The amorphization of

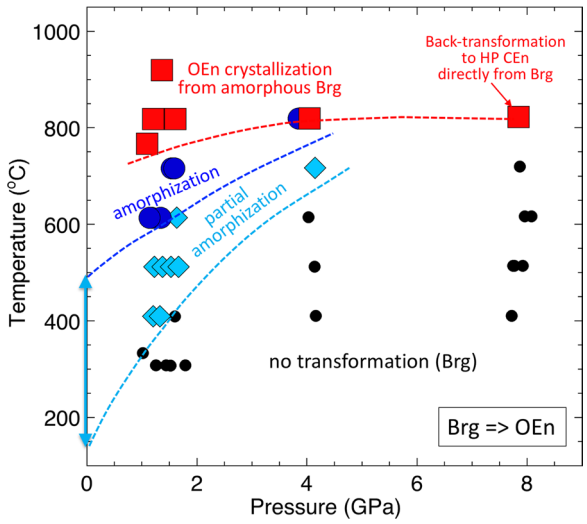


**Fig. 5** P–T conditions for the back-transformation in bridgmanite. Bridgmanite (Brg, black circles) becomes amorphous (partially, blue diamonds; completely, blue circles), followed by orthoenstatite crystallization (OEn, red squares) with increasing temperatures at ~ 1–4 GPa, and directly back-transforms to high-P clinoenstatite (HP CEn) at ~ 8 GPa. A double-headed arrow indicates the temperature condition for partially amorphization observed in Durben and Wolf (1992)

lingunite proceeded at 610–720 °C, which was confirmed by the decrease in peak intensity in lingunite and the increase in amorphous halo (Fig. 9a). However, before completing the amorphization, the plagioclase crystallization started at ~ 720–820 °C with decreasing the halo (Fig. 9b). The diffraction peaks in lingunite eventually disappeared in ~ 7 min at 820 °C.

### 3.2 Analysis of kinetic data

In the back-transformation experiments of ringwoodite, we measured transformed volume fraction as a function of time at six different P–T conditions as shown in Fig. 10a,b. The transformed fraction was estimated based on the integrated intensities of several diffraction peaks. The kinetic data were analyzed by using the Avrami rate equation as follows:

$$V = 1 - \exp\left(-kt^n\right) \tag{1}$$

where $V$ is transformed volume fraction, $k$ and $n$ are constants, and $t$ is time. Kinetic parameters in the rate Eq. (1) were estimated from nonlinear least-squares fitting. The obtained $k$ and $n$ values are listed in Table 1. Plots of ln ln $\{1/(1-V)\}$ against ln $(t)$ are also shown in Fig. 10c, in which the intercept and the slope are corresponding to the values of ln $k$ and $n$, respectively.

The obtained $n$ values in the back-transformation from ringwoodite to olivine are nearly 1 (~ 0.9–1.1) although runs M2716 and M2932 show relatively small $n$ values ~ 0.7 probably due to the lack of the kinetic data at the initial stage. This suggests that the site saturation occurs at the early stage of the transformation under the conditions far from the equilibrium boundary (i.e., large free energy differences), followed by one-dimensional interface-controlled growth (e.g., Cahn 1956; Rubie et al. 1990). This is consistent with the back-transformation microstructures observed in Fig. 4b. In this case, the growth rate $\dot{x}$ can be deduced from the rate constant $k$ with the $n$ value of 1 using the following equation:

$$k_{n=1} = 2S\dot{x}, \tag{2}$$

where $S$ is the grain-boundary area per unit volume. $S$ can be expressed $3.35/d$, where $d$ is the grain size of the parental phase (8.9 μm). The estimated growth rate is listed in Table 1.

In the back-transformation experiments of bridgmanite, amorphization first occurs before crystallization of orthoenstatite at least up to ~ 4 GPa. We could not obtain the kinetic data on the amorphization, but succeeded to measure the crystallization kinetics of enstatite from amorphous bridgmanite at 3 different P–T conditions. We also obtained kinetic data of the direct back-transformation from bridgmanite to high-P clinoenstatite at 7.9 GPa and 820 °C. These kinetic data were analyzed by using the rate Eq. (1) in a similar way to the case of ringwoodite, as summarized in Fig. 11 and Table 2.

In contrast to the olivine formation from ringwoodite, the $n$ value for the orthoenstatite crystallization from amorphous bridgmanite is larger (~ 1.8–2.0), implying that not only the growth but also the nucleation process controls the overall reaction rate. In the ringwoodite to olivine back-transformation, the change in the chemical free energy is very large under low-pressure conditions. This enhances the nucleation process by the decrease in the activation energy for nucleation, thus leading to the site saturation at the early stage (i.e., growth-controlled transformation). The difference in the chemical free energy is also thought to be very large between bridgmanite and orthoenstatite; however, the presence of the intermediate amorphous phase would reduce the difference available for the orthoenstatite nucleation. The interfacial energy between the enstatite crystal and amorphous phase may also affect the nucleation kinetics. Owing to these reasons, the bridgmanite amorphization possibly inhibited the enstatite nucleation, resulting in the increase in $n$ values for overall reaction kinetics.

On the other hand, the kinetics of the direct back-transformation from bridgmanite to high-P clinoenstatite without amorphization is rather different as shown in

**Table 2** P–T–t conditions and estimated values of kinetic parameters for the back-transformation in bridgmanite

| Run No. | Pressure (GPa) | Temperature (°C) | Duration (s) | Phase[1] | *n* | ln *k* | ln *k* for the averaged *n* value[2] |
|---|---|---|---|---|---|---|---|
| OEn formation from amorphous bridgmanite | | | | | | | |
| M2718 | 1.0 | 330 | 410 | Brg | | | |
| | 1.1 | 615 | 620 | Complete amo | | | |
| | 1.1 | 765 | 1655 | OEn | 2.02 | − 13.9 | − 13.1 (0.07) |
| M2619 | 1.3 | 310 | 290 | Brg | | | |
| | 1.2 | 410 | 410 | Partial amo | | | |
| | 1.2 | 510 | 700 | Partial amo | | | |
| | 1.2 | 615 | 1560 | Complete amo | | | |
| M2621 | 1.4 | 310 | 265 | Brg | | | |
| | 1.3 | 410 | 425 | Partial amo | | | |
| | 1.4 | 510 | 375 | Partial amo | | | |
| | 1.3 | 615 | 450 | Complete amo | | | |
| | 1.2 | 820 | 485 | OEn | 1.89 | − 5.90 | − 5.76 (0.22) |
| backtra11 | 1.5 | 310 | 560 | Brg | | | |
| | 1.5 | 510 | 2050 | Partial amo | | | |
| | 1.5 | 715 | 1620 | Complete amo | | | − 18.4[#] |
| backtra12 | 1.8 | 310 | 510 | Brg | | | |
| | 1.6 | 410 | 460 | Brg | | | |
| | 1.7 | 510 | 470 | Partial amo | | | |
| | 1.6 | 615 | 1250 | Partial amo | | | |
| | 1.6 | 715 | 1400 | Complete amo | | | |
| | 1.6 | 820 | 720 | OEn | No kinetic data obtained | | |
| | 1.4 | 920 | 840 | OEn | | | |
| M2618 | 4.2 | 410 | 130 | Brg | | | |
| | 4.1 | 510 | 460 | Brg | | | |
| | 4.0 | 615 | 305 | Brg | | | |
| | 4.2 | 720 | 465 | Partial amo | | | |
| | 3.9 | 820 | 30 | Complete amo | | | |
| | 4.0 | 820 | 690 | OEn | 1.79 | − 9.10 | − 9.61 (0.08) |
| Bridgmanite to HP-CEn transformation | | | | | | | |
| M2613 | 7.7 | 410 | 440 | Brg | | | |
| | 7.8 | 514 | 485 | Brg | | | |
| | 8.0 | 617 | 420 | Brg | | | |
| | 7.9 | 720 | 265 | Brg | | | |
| M2715 | 7.8 | 515 | 1165 | Brg | | | |
| | 8.1 | 620 | 1560 | Brg | | | |
| | 7.9 | 820 | 2515 | HP CEn | 0.40 | − 2.18 | |

[1] Brg, bridgmanite; amo, amorphization; OEn, orthoenstatite; HP CEn, high-P clinoenstatite

[2] The uncertainties in rate constant are listed in parentheses

[#] The maximum *k* value was estimated (see text)

(See figure on next page.)

**Fig. 6** Changes of XRD patterns during the back-transformation in bridgmanite. **a** Amorphization of bridgmanite with increasing temperatures from 410 to 610 °C at ~ 1.2 GPa (Run M2619). **b** Crystallization of orthoenstatite from amorphous bridgmanite at 1.1 GPa and 770 °C (Run M2718). **c** Amorphization of bridgmanite occurred in 30 s, followed by orthoenstatite crystallization at 4.0 GPa and 820 °C (Run M2618). **d** Direct back-transformation from bridgmanite to high-P clinoenstatite without amorphization at 7.9 GPa and 820 °C (Run M2715). St: stishovite, Mj: majorite, *: unknown

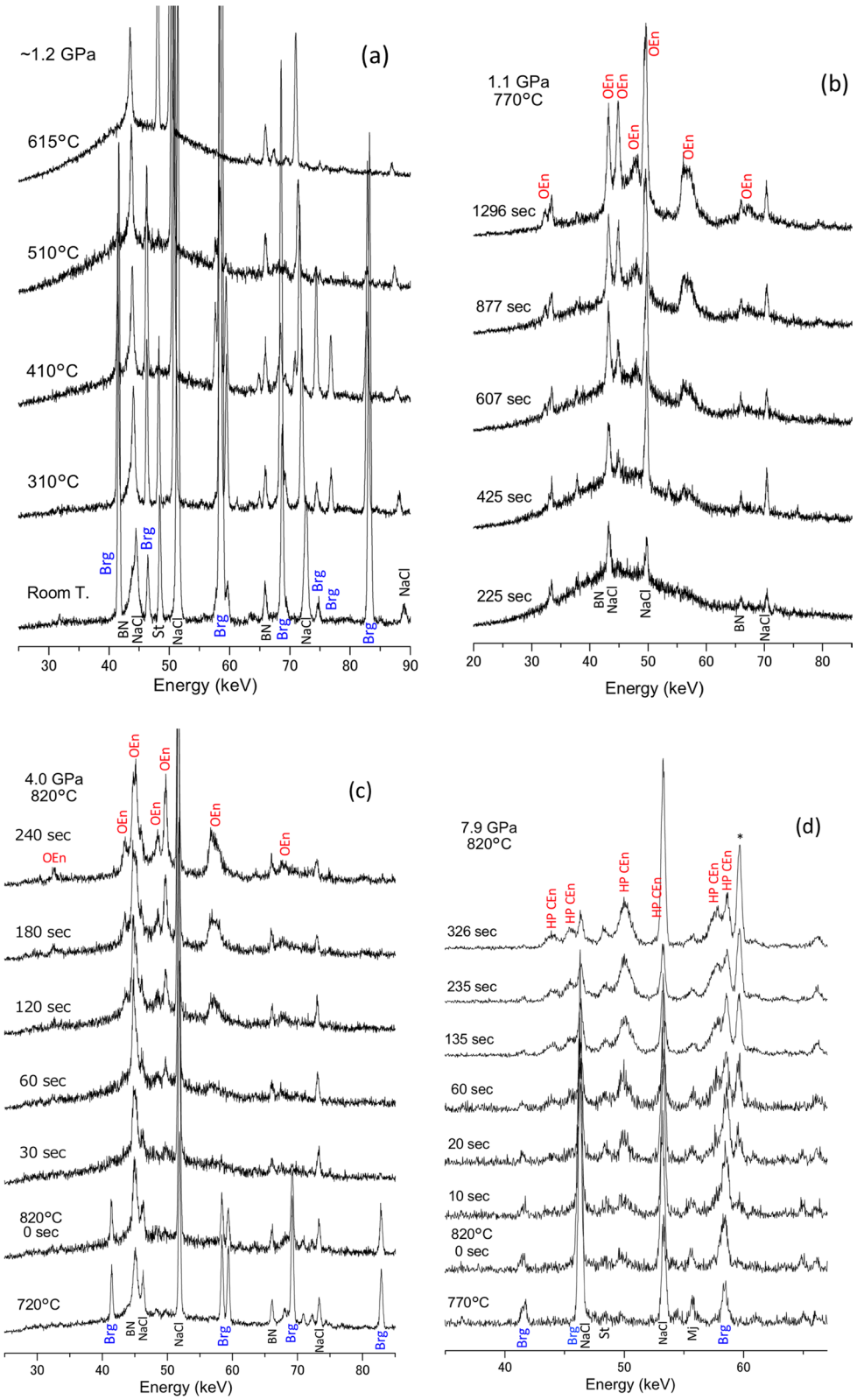


**Fig. 6** (See legend on previous page.)

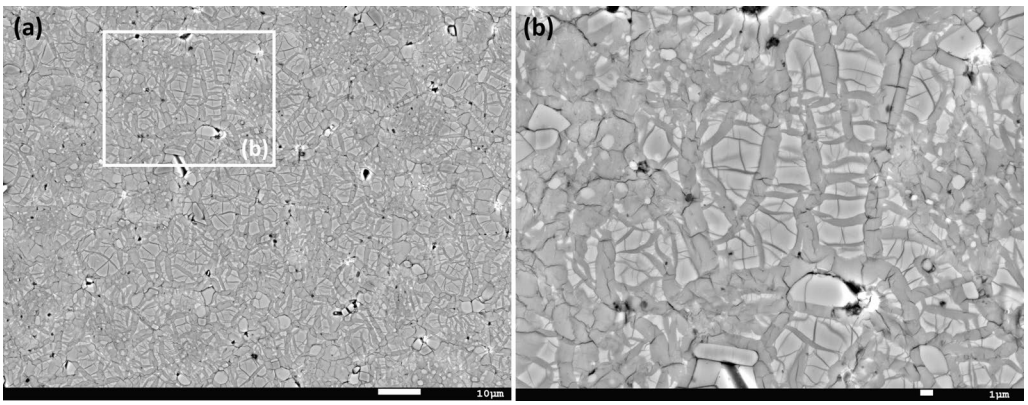


**Fig. 7** BSE images showing back-transformation microstructures from bridgmanite to high-P clinoenstatite. **a** The back-transformation occurred in darker regions by both inter- and intra-crystalline processes at 7.9 GPa and 820 °C (Run M2715). **b** A high-magnification image of a white-colored box in **a**

Fig. 11. The $n$ value is very small (~0.5), suggesting that the nucleation is thought to be very fast relative to the growth process in this reaction. This indirectly supports the interpretation that the enstatite nucleation is inhibited due to the formation of the intermediate amorphous phase.

### 3.3 Pressure and temperature dependences of the back-transformation rate

The growth rate data for the back-transformation in ringwoodite were analyzed by using the rate equation for the interface-controlled growth as follows:

$$\dot{x} = AT\exp\left(-\frac{H^*}{RT}\right)\left[1-\exp\left(-\frac{\Delta G_r}{RT}\right)\right] \quad (3)$$

where $A$ is constant, $H^*$ is activation enthalpy, $\Delta G_r$ is the free energy change of the transformation, $R$ is gas constant, and $T$ is absolute temperature (Turnbull 1956). The activation enthalpy is described as $H^* = E^* + PV^*$, where $E^*$ is activation energy, $P$ is pressure, and $V^*$ is activation volume. For calculation of $\Delta G_r$, the thermodynamic data of Kojitani et al. (2017) for $Mg_2SiO_4$, and Akaogi et al. (1989) and Fabrichnaya et al. (2004) for $Fe_2SiO_4$ were used. We applied symmetric regular solution model by using nonideal parameters of Kojitani and Akaogi (1994) for olivine and Akaogi et al. (1989) for ringwoodite. Calculated values of $\Delta G_r$ are listed in Table 1. This rate equation was fitted to the growth rate data listed in Table 1 by a least-squares procedure, which yields $E^* = 456$ kJ/mol and $V^* = 6.9$ cm$^3$/mol. The results of the fitting are summarized in Fig. 12a and Table 3. Based on these kinetic parameters with Eqs. (1)–(3), we can estimate the growth-controlled back-transformation rate in ringwoodite at a given P, T, and grain size condition.

The $n = 1$ kinetics has also been reported in the back-transformation of $Mg_2SiO_4$ wadsleyite in air, from which the growth rate can be deduced based on the parental grain size of ~ 1 μm (Reynard et al. 1996; Hu and Sharp 2017). We analyzed these data based on the Eq. (3) assuming the same activation volume determined in this study (Fig. 12, Table 3). $\Delta G_r$ was estimated from $\Delta P \Delta V$, where $\Delta P$ is the pressure difference from the equilibrium boundary, and $\Delta V$ is molar volume change of the reaction. For calculation of $\Delta P$, we used the equilibrium olivine-wadsleyite phase boundary in $Mg_2SiO_4$ (Morishima et al. 1994). Figure 12 indicates that, although the temperature dependence is

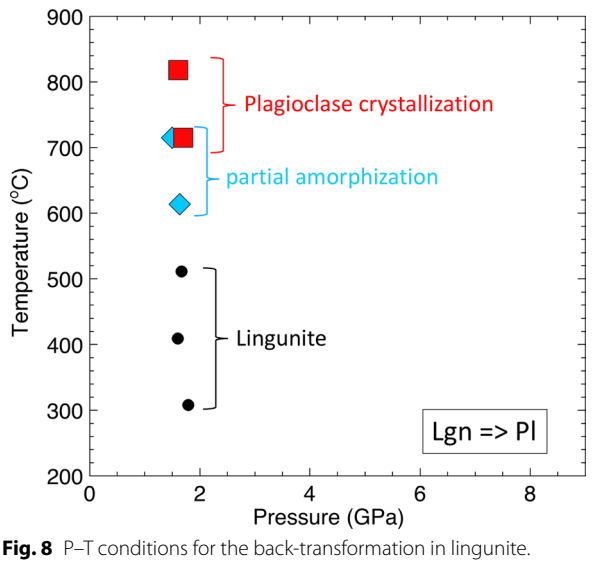


**Fig. 8** P–T conditions for the back-transformation in lingunite. Partial amorphization and plagioclase crystallization proceeded with increasing temperatures (Run backtra12)

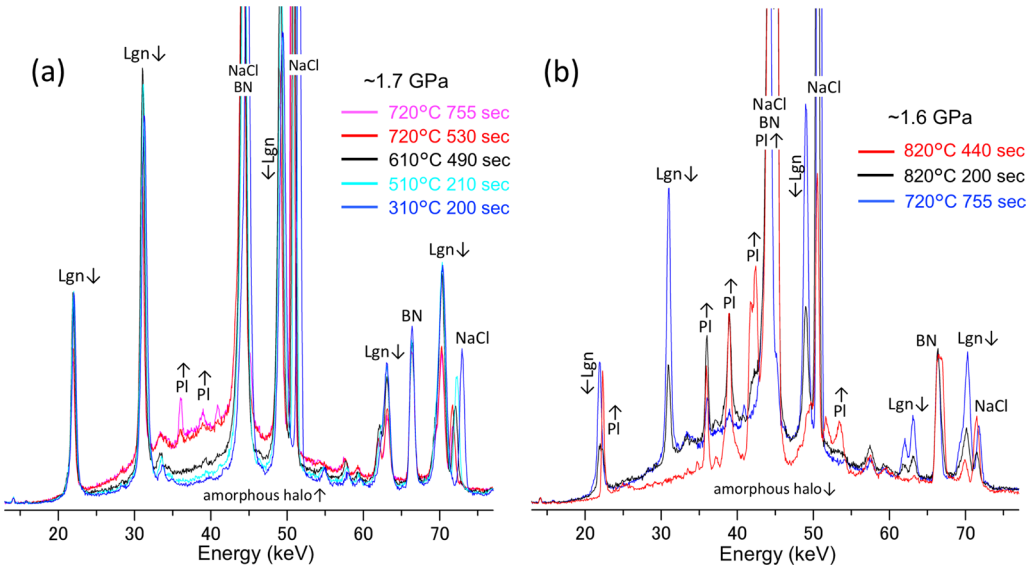


**Fig. 9** Changes of XRD patterns during the back-transformation in lingunite (Run backtra12, Lgn: lingunite, Pl: plagioclase). The arrows indicate the change of the peak intensity with temperature or time. **a** Lingunite amorphization occurred with increasing temperature at ~ 1.7 GPa and 610–820 °C, and plagioclase crystallization started before its completion. **b** Crystallization of plagioclase proceeded with decreasing amorphous halo at ~ 1.6 GPa and 820 °C

similar, the growth rate in the present study is about 4 orders of magnitude lager than those obtained in Reynard et al. (1996) even considering the pressure effect. Interface mobility is thought to be similar between the olivine-wadsleyite and the olivine-ringwoodite interphase boundary. It is unlikely that differences in iron content have such large effects on the growth kinetics. The reason for the large difference in the growth rate may be originated from water contained in the starting ringwoodite (~ 1400 wt. ppm $H_2O$). Effects of water on the interface kinetics are significant as reported in previous studies (Hosoya et al. 2005; Nishihara et al. 2006). Hosoya et al. (2005) have shown that the growth rate in the olivine–wadsleyite transformation is proportional to OH content to the power of 3.2. Considering this water dependent kinetics, the large differences in growth rates can be explained assuming that the sample of Reynard et al. (1996) is relatively dry ~ 70 wt. ppm $H_2O$ (Fig. 12).

We also examined pressure and temperature dependences of the rate constant $k$ for orthoenstatite crystallization from amorphous bridgmanite by the following Arrhenius type equation:

$$k = k_0 \exp\left(-H^*/RT\right) \tag{4}$$

where $k_0$ is constant. We obtained the $k$ data at three different P–T conditions (1.1–4.0 GPa and 765–820 °C) with the averaged $n$ value of 1.9 (Table 2). Additionally, we also preliminarily observed that the orthoenstatite crystallization did not start in 27 min at 1.5 GPa and 715 °C (Run backtra 11). We estimated the maximum $k$ value of this run assuming the $n = 1.9$ kinetics (Table 2). Thus, a total of four data points were used to estimate kinetic parameters in Eq. (4) as summarized in Fig. 12b and Table 3. The activation energy for the orthoenstatite crystallization from amorphous bridgmanite is much larger than that for the olivine formation from ringwoodite. This is probably because the rate constant $k$ for the orthoenstatite crystallization involves both nucleation and growth processes as discussed above.

Knittle and Jeanloz (1987) reported much faster kinetics with smaller activation energy of ~ 70 kJ/mol for the back-transformation of bridgmanite to enstatite at ambient pressure. They did not obtain time-dependent kinetic data in most of runs. Although the $n = 3$ kinetics was obtained in a limited condition, it was not enough to estimate the quantitative temperature dependence of the $k$ value. The back-transformation to enstatite was observed at much lower temperatures of ~ 520–610 °C in 6–24 h in their experiment. Extrapolations of our kinetic data (Fig. 12b) to their condition (0 GPa and 600 °C) indicate that more than 1000 h are necessary for the 10% enstatite crystallization. Additionally, they observed bridgmanite even at ~ 550 °C for 6 h and no glass in any samples, which is inconsistent with the amorphization behavior observed in previous studies (Durben and Wolf 1992; Wang et al. 1992) and this study (Fig. 5). Durben and Wolf (1992) showed that

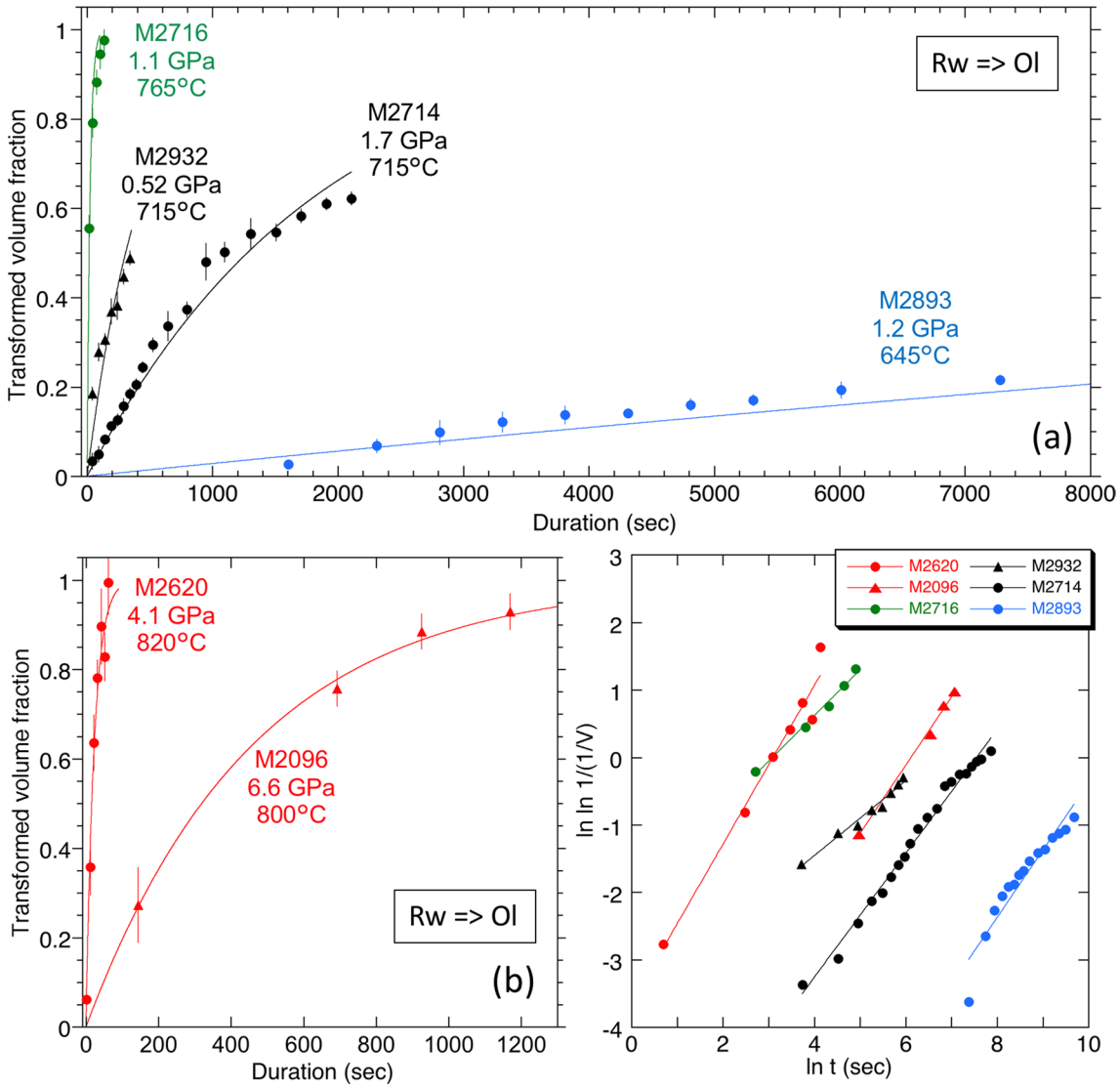


**Fig. 10** Back-transformation kinetics from ringwoodite to olivine. **a**, **b** Transformation-time data at six different P–T conditions. Curves obtained by least-squares fits of the kinetic data to Eq. (1) are also shown. Note that Run M2893 lasted 18,340 s until the transformed fraction reached ~ 34 vol% although kinetic data with $t > 8000$ s is not shown. **c** Plots of ln ln {1/(1 − *V*)} against ln (*t*). The intercept and the slope are corresponding to the values of ln *k* and *n*, respectively

thermally induced vitrification of bridgmanite begins near 130 °C and is complete by ~ 480 °C on the basis of a Raman spectroscopic study, which is in good agreement with extrapolations of our results on the amorphization temperatures to ambient pressure condition (Fig. 5). Knittle and Jeanloz (1987) synthesized the starting bridgmanite in a diamond-anvil cell, whereas a KAWAI-type apparatus was used in Durben and Wolf (1992) and our study, which may affect the back-transformation behaviors through the differences in grain size and/or crystallinity.

### 3.4 Back-transformations during the post-shock stage in shocked meteorites

In the present study, the back-transformation kinetics was examined in the timescale from several tens of seconds to a few hours (Figs. 10, 11). In order to discuss different timescales in planetary collision and diamond transportation, the obtained kinetic parameters were used to estimate pressure and temperature kinetic boundaries in a given timescale appropriate for each event.

P–T history during the shock event have been discussed in some shocked meteorites based on thermal

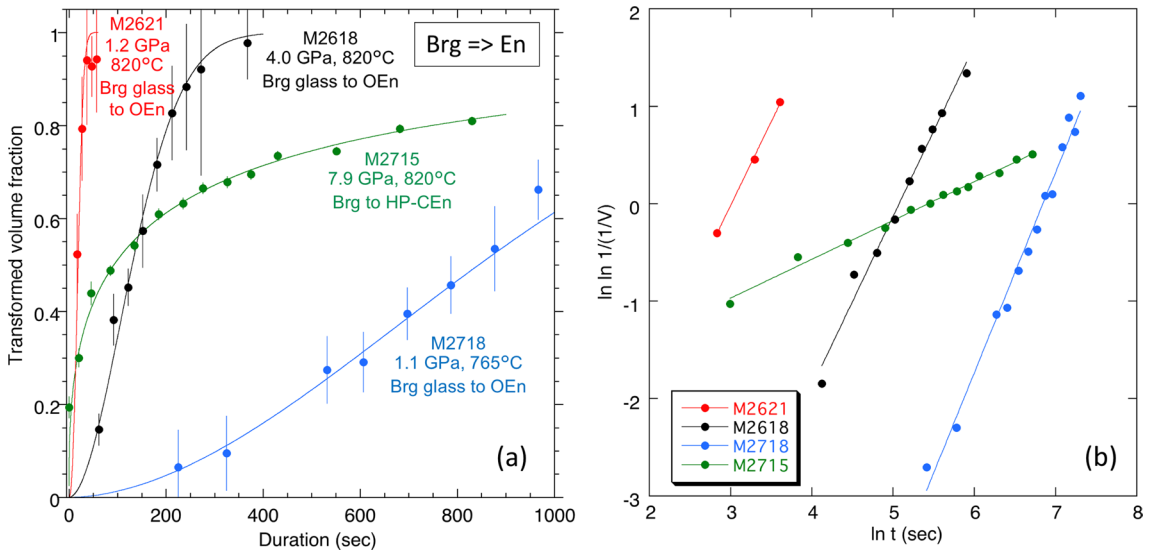


**Fig. 11** Back-transformation kinetics in bridgmanite. **a** Transformation-time data for orthoenstatite crystallization from amorphous bridgmanite (red, black, and blue circles), and for direct back-transformation from bridgmanite to high-P clinoenstatite (green circles). **b** Plots of ln ln {1/(1 − *V*)} against ln (*t*). The *n* values (slope) are different depending on the reaction

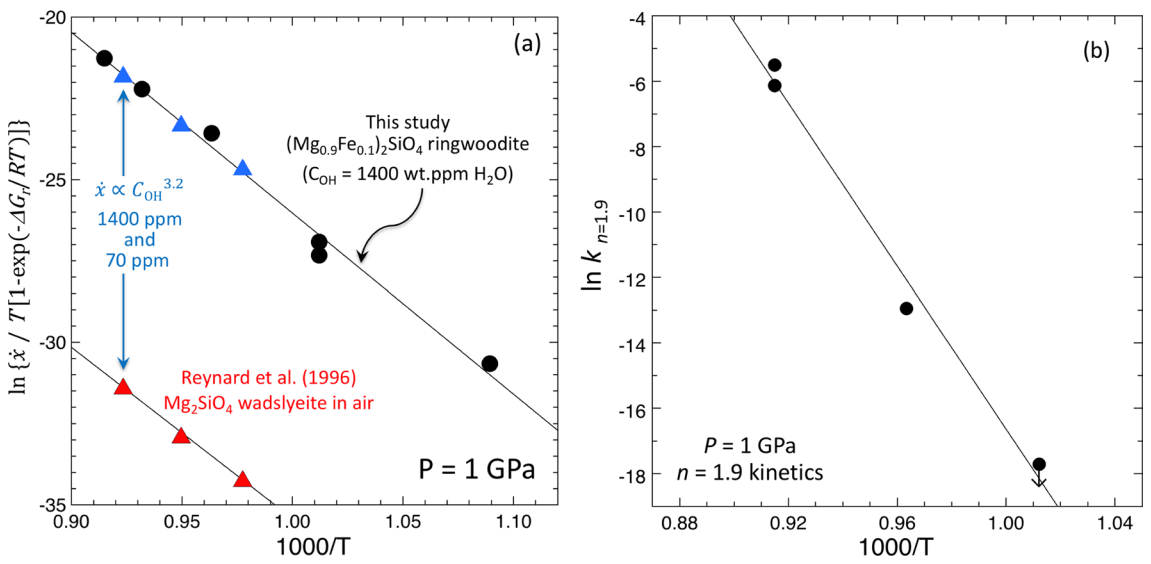


**Fig. 12** Analysis of pressure and temperature dependences of the back-transformation rate. For plotting purposes, the data are plotted after corrections to the pressure of 1 GPa using the activation volume determined in this study. Obtained kinetic parameters are summarized in Table 3. **a** Fits of the growth rate data in the ringwoodite-olivine (black circles; this study) and in the wadsleyite-olivine (red triangles; Reynard et al. 1996; Hu and Sharp 2017) back-transformations to Eq. (3). Large discrepancies between these growth rate data correspond to the difference in water contents by about 20 times (red and blue triangles) considering the water content exponent of 3.2 (see text). **b** Fits of the *k* data in the orthoenstatite crystallization from amorphous bridgmanite to Eq. (4)

modelling considering the distributions of high-pressure phases in shock vein and host rock. Duration of the pressure pulse experienced in shocked meteorites has been estimated to be ~ 0.01 s to a few seconds (e.g., Ohtani et al. 2004; Beck et al. 2005; Xie and Sharp 2007). After the shock pulse release, pressure and temperature

**Table 3** P and T dependences of the rate constant *k* and growth rate

| Reaction | ln $k_0$ | $E^*$ (kJ/mol) | $V^*$ ($cm^3$/mol) |
|---|---|---|---|
| Ringwoodite to olivine[1] | 29.6 (4.1) | 456 (34) | 6.9 (1.0) |
| Wadsleyite to olivine[2] | 17.2 (2.5) | 431 (22) | 6.9 (fixed) |
| Brg glass to OEn[3] | 108 (10) | 1025 (88) | 10.7 (3.4) |

The uncertainties in kinetic parameters are listed in parentheses

[1] Equation (3) was fitted to the growth rate data obtained in this study

[2] Equation (3) was fitted to the growth rate data obtained in Reynard et al. (1996) and Hu and Sharp (2017) assuming the same activation volume as that of the ringwoodite to olivine transformation

[3] Equation (4) was fitted to the rate constant *k* data obtained in this study

suddenly drop by the adiabatic decompression, followed by the cooling at ambient pressure in longer timescales (~ $10^0$–$10^2$ s) by thermal conduction in the post-shock annealing stage (e.g., Ohtani et al. 2004; Hu and Sharp 2017). Ringwoodite is present in fragments in shock vein and host rock in the vicinity of shock vein with having granular and lamellar textures (e.g., Tomioka and Miyahara 2017). The grain sizes and lamellar widths of ringwoodite are ~ 0.5–2 μm (e.g., Ohtani et al. 2004; Xie and Sharp 2007; Miyahara et al. 2008). Our experiments suggested that the back-transformation from ringwoodite to olivine is growth-controlled process. To discuss the back-transformation of ringwoodite considering these points, we estimated kinetic boundaries for the 1 μm growth of olivine from ringwoodite in the timescale of 0.1–100 s (Fig. 13a).

The back-transformation rate in shocked meteorites may be influenced by water; however, previous studies on water contents of nominally anhydrous minerals in shocked meteorites have been limited. Hallis et al. (2017) have reported that ringwoodite grains in Tissint Martian meteorite contain up to 1132 wt. ppm $H_2O$. This water content is similar to that in our starting material. It is thought that constituent minerals in L5/6 ordinary chondrites are relatively dry compared to those in Tissint Martian meteorite. Therefore, we plotted two kinetic boundaries based on the parameters deduced from our experiments and Reynard et al. (1996) (Table 3), which may represent wet and dry conditions in shocked meteorites, respectively.

To avoid the back-transformation, the P–T path should be below the kinetic boundary during both the adiabatic decompression and the post-shock annealing stages. The temperature–time history during the post-shock stage depends on several factors such as the post-shock temperature, the shock melt vein thickness, and the distance from the vein. We plotted typical three thermal models (A–C) proposed in previous studies (Ohtani et al. 2004; Hu and Sharp 2017) in Fig. 13a, suggesting possible variations of the back-transformation of ringwoodite in shocked meteorites. Ringwoodite at 20 μm in the host from a shock vein of 0.8–1.0 mm thickness (case A, Hu and Sharp 2017) can survive over the post-shock annealing stage if it is under dry condition, whereas ringwoodite at 100 μm in the host from a shock vein of 2.0 mm thickness (case B, Ohtani et al. 2004) can survive even under wet condition like Tissint Martian meteorite. The back-transformation cannot be avoided along the temperature–time path expected in fragments in shock veins of 0.8–1.0 mm thickness (case C, Hu and Sharp 2017). Thus, thermal history of shock events including the post-shock stage can be uniquely constrained by considering both forward and backward olivine-ringwoodite transformations.

Figure 13b shows the back-transformation processes expected in bridgmanite from our experimental data. Crystalline bridgmanite have been found in the clast in the shock vein and host rock in L5–6 ordinary chondrites, usually coexisting with amorphous bridgmanite (Tomioka and Fujino 1997; Tschauner et al. 2014). Sharp et al. (1997) have reported the presence of amorphous bridgmanite in the shock vein matrix. In Martian meteorites, crystalline and amorphous bridgmanite have been found in the post-spinel decompositional assemblage (Miyahara et al. 2011), and the back-transformation to enstatite have also been reported (Miyahara et al. 2019). For the preservation of crystalline bridgmanite during adiabatic decompression to ambient pressure, it is necessary to avoid complete amorphization and the direct back-transformation to high-P clinoenstatite.

If we adopt thermal models (A–C) discussed above to Fig. 13b, it turns out that the preservation of crystalline bridgmanite during the post-shock stage is rather difficult. Complete amorphization is unavoidable in bridgmanite by the post-shock annealing at ~ 700 °C for 100 s in the case B. The higher temperature paths of case A and C would result in the back-transformation to high-P clinoenstatite (and to low-P clinoenstatite). However, kinetic behaviors in shorter timescales than 10 s remains unclear for both processes as we could not determine quantitative kinetics yet. Additionally, it has been suggested that volume expansion associated with amorphization produces transformation stress in the residual crystalline bridgmanite (Durben and Wolf 1992). They observed residual Raman shift in crystalline bridgmanite that is comparable to a hydrostatic pressure of ~ 1.3 GPa. This effect may avoid the complete amorphization during the post-shock annealing stage.

Lingunite, that is a hollandite-type high-pressure polymorph of $NaAlSi_3O_8$-rich plagioclase, has been found in shock veins in ordinary chondrites (e.g., Tomioka et al. 2000; Gillet et al. 2000). Amorphous plagioclase is

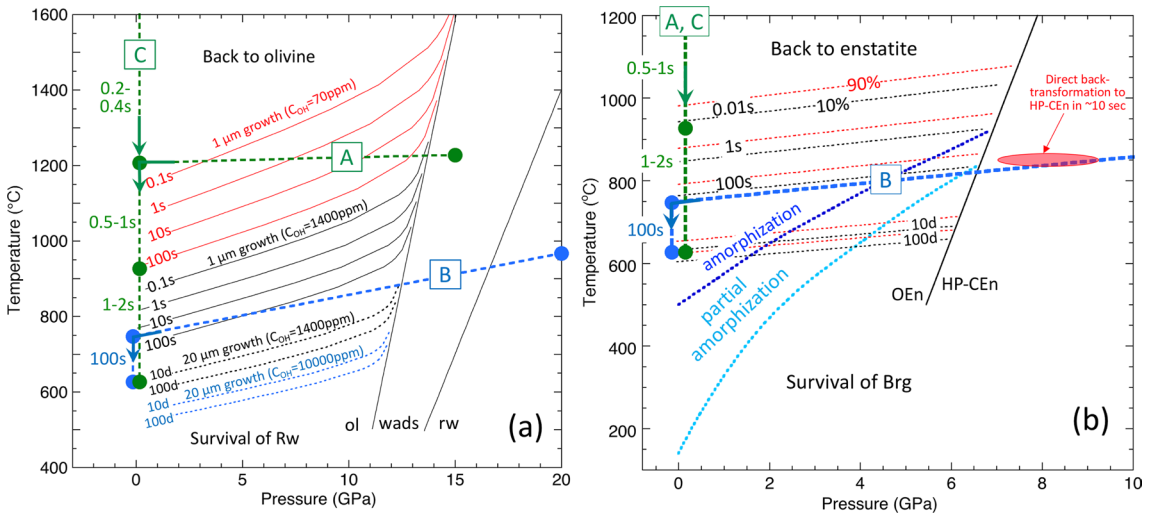


**Fig. 13** Back-transformations in timescales of 0.1–100 s and 10–100 days expected in shocked meteorites and diamond inclusions, respectively. **a** Kinetic boundaries for the 1 μm and 20 μm growth of olivine from ringwoodite including effects of water. **b** Amorphization conditions in bridgmanite and kinetic boundaries for 10% and 90% crystallization of orthoenstatite from amorphous bridgmanite. Typical three thermal models (A–C) during the post-shock annealing stage are shown in bold dashed lines. (A) 20 μm inside the host with vein thickness of 0.8–1 mm, $P_{max}$ ~ 15 GPa and post-shock $T$ ~ 1500 K (Hu and Sharp 2017). (B) 100 μm inside the host with vein thickness of 2 mm, $P_{max}$ ~ 20 GPa and post-shock $T$ ~ 1240 K (Ohtani et al. 2004). (C) 200 μm clast in the shock vein of 0.8–1 mm thickness, $P_{max}$ ~ 15 GPa and post-shock $T$ > 2000 K (Hu and Sharp 2017)

present in the vicinity of lingunite; however, there have been no reports on the fine-grained plagioclase that may be back-transformed from lingunite. Although the stability field of the hollandite-type phase in this chemical composition has not been confirmed by phase equilibrium studies, it has been suggested that the metastable formation from amorphous plagioclase is a possible origin of lingunite in shocked chondritic meteorites (Kubo et al. 2017). The present study showed that re-amorphization of lingunite proceeds at slightly higher temperatures (~ 600–700 °C) compared to the bridgmanite case. Plagioclase crystallization, that occurs at ~ 700–800 °C in several minutes, requires higher temperatures in shorter time scales of shock event. Formation and survival of lingunite in shocked meteorites would give another important constraint on shock history although quantitative kinetics are needed to discuss further details.

### 3.5 Back-transformations during the diamond transportation from the deep Earth

The timescale of transportation of deep diamonds from mantle transition zone to the surface of the Earth is still unclear. Until the kimberlite eruption has brought diamonds at the final stage, they might be transferred to the upper mantle by the long-time mantle flow (Harte and Cayzer 2007), or the rapid kimberlite ascent might bring them directly from deeper mantle (Ringwood et al. 1992). Nishi et al. (2010) compared the back-transformation textures in majoritic garnet observed in diamond inclusion with those in laboratory kinetics experiments and suggested that diamonds have been transported directly from deep mantle by the rapid kimberlite magma in ~ 190–2000 h at 1200–1400 °C. We discuss survival of high-pressure minerals during the diamond transportation considering this timescale in Fig. 13.

There has been only one report on the ringwoodite inclusion in diamond (Pearson et al. 2014). It contains ~ 14,000–15,000 wt. ppm $H_2O$, and its grain size is ~ 40 μm. We plotted kinetic boundaries for the 20 μm growth of olivine from ringwoodite in the timescales of 10–100 days (Fig. 13a). Assuming the water content exponent of 3.2 for the growth rate (Hosoya et al. 2005), kinetic boundaries with different water contents ($C_{OH}$ = 1400 and 10,000 wt. ppm $H_2O$) are shown. Figure 13a indicates that preservation of ~ 40 μm hydrous ringwoodite during the kimberlite magma ascent is quite difficult. It requires lower temperatures than ~ 600 °C. Because it is unlikely that such low temperatures were realized when erupting kimberlite magma, the internal pressure in the diamond must be high enough to prevent the hydrous ringwoodite from the back-transformation. Majoritic garnet can be survived to the Earth surface by kimberlite eruption due to the slow back-transformation kinetics as shown in Nishi et al. (2010), but ringwoodite cannot be preserved in diamond without the help of residual stress.

On the other hand, (Mg, Fe)$SiO_3$ bridgmanite has not been found in diamond so far. Several studies have

suggested super-deep diamonds that include the lower-mantle assemblage of ferropericlase and enstatite inverted from the former bridgmanite (e.g., Hayman et al. 2005). Our study clearly shows that both crystalline and amorphous bridgmanite cannot be preserved, but the back-transformation to high-P clinoenstatite likely occurs along P–T–t paths expected for the transportation of diamond by kimberlite magma. Even if bridgmanite is amorphized during the diamond ascent, it seems to have enough time to crystallize to enstatite at higher than 600 °C (Fig. 13b). This is in agreement with the presence of enstatite instead of the amorphous phase as the former bridgmanite in super-deep diamonds.

## 4 Summary

Survival of high-pressure minerals in shocked meteorites and diamond inclusions provide important constraints on the P–T–t history of planetary collisions and diamond transportation by considering the back-transformation kinetics. High-pressure in situ X-ray observations revealed that ringwoodite directly back-transforms to olivine by grain-boundary nucleation and growth mechanisms. The obtained kinetics can explain the varieties of the back-transformation along the possible P–T–t paths in the post-shock stage of shocked meteorites considering the water effects. Preservation of the hydrous ringwoodite during diamond transportation from the deep Earth is quite difficult without the help of residual stress. Bridgmanite first becomes amorphous state followed by crystallization of orthoenstatite at ~ 1–4 GPa, and directly back-transforms to high-P clinoenstatite at ~ 8 GPa. The amorphization also occurs in lingunite at ~ 1.5 GPa, and plagioclase crystallization starts before the complete amorphization. Our results are consistent with the presence of enstatite instead of the amorphous phase as the former bridgmanite in super-deep diamonds, however cannot explain the presence of crystalline bridgmanite in shocked meteorites. It is necessary to investigate detailed processes of amorphization in much shorter timescale to assess this issue.

**Acknowledgements**
This paper is dedicated to late Prof. Ahmed El Goresy who made a great contribution to the field of meteoritical sciences. We deeply appreciate for his interest and helpful comments on our experimental studies. We thank K. Shimada, S. Yamanouchi, D. Wakabayashi, and M. Ikehara for their assistance with experiments, M. Nishi and Y. Tsubokawa for helpful discussion, and H. Kojitani for the calculation of thermodynamic properties. X-ray diffraction experiments using synchrotron radiation were carried out at AR-NE5C of the Photon Factory (proposal no. 2016G598) and at BL04B1 of SPring-8 (proposal nos. 2016B1358, 2018B1363 and 2019A1487).

**Author contributions**
TK and MM proposed the topic, and TK and KK conceived and designed the study. TK, KK, MI, YT, and YH carried out the experimental study. TK, KK, and MM analyzed the data and helped in their interpretation. TK wrote the manuscript. All authors read and approved the final manuscript.

**Funding**
This work was partially supported by MEXT/JSPS KAKENHI Grant Numbers JP18H01269 and JP18H05232.

**Availability of data and materials**
The datasets supporting the conclusions of this article are included within the article.

## Declarations

**Ethical approval**
This article does not contain any studies with human participant or animals performed by any of the authors.

**Competing interests**
The authors declare that they have no competing interests.

**Author details**
[1]Department of Earth and Planetary Sciences, Faculty of Sciences, Kyushu University, Fukuoka 819-0395, Japan. [2]Department of Earth and Planetary Sciences, Graduate School of Sciences, Kyushu University, Fukuoka 819-0395, Japan. [3]Japan Synchrotron Radiation Research Institute, Hyogo 679-5198, Japan. [4]Graduate School of Advanced Science and Engineering, Hiroshima University, Higashi-Hiroshima 739-8526, Japan.

Received: 31 October 2021 Accepted: 1 April 2022
Published online: 21 April 2022

**References**

Akaogi M, Ito E, Navrotsky A (1989) Olivine-modified spinel- spinel transitions in the system $Mg_2SiO_4$–F%$SiO_4$: calorimetric measurements, thermochemical calculation, and geophysical application. J Geophys Res 94:15671–15685

Akashi A, Nishihara Y, Takahashi E, Nakajima Y, Tange Y, Funakoshi K (2009) Orthoenstatite/clinoenstatite phase transformation in $MgSiO_3$ at high-pressure and high-temperature determined by in situ X-ray diffraction: implications for nature of the X discontinuity. J Geophys Res. https://doi.org/10.1029/2008JB005894

Angel RJ, Chopelas A, Ross NL (1992) Stability of high-density clinoenstatite at upper-mantle pressures. Nature 358:322–324

Beck P, Gillet P, El Goresy A, Mostefaoui S (2005) Timescales of shock processes in chondritic and Martian meteorites. Nature 435:1071–1074

Brown JM (1999) The NaC1 pressure standard. J Appl Phys 86:5801–5808

Cahn JW (1956) The kinetics of grain boundary nucleated reactions. Acta Metall 4:449–459

Durben DJ, Wolf GH (1992) High-temperature behavior of metastable $MgSiO_3$ perovskite: a Raman spectroscopic study. Am Min 77:890–893

Fabrichnaya O, Saxena SK, Richet P, Westrum EF (2004) Thermodynamic data, models and phase diagrams in multicomponent oxide systems. Springer, Berlin

Fukimoto K, Miyahara M, Sakai T, Ohfuji H, Tomioka N, Kodama Y, Ohtani E, Yamaguchi A (2020) Back-transformation mechanisms of ringwoodite and majorite in an ordinary chondrite. Meteorit Planet Sci 55:1749–1763

Gillet P, Chen M, Dubrovinsky L, El Goresy A (2000) Natural $NaAlSi_3O_8$-hollandite in the shocked sixiangkou meteorite. Science 287:1633–1636

Hallis LJ, Huss GR, Nagashima K, Taylor GJ, Stöffler D, Smith CL, Lee MR (2017) Effects of shock and Martian alteration on Tissint hydrogen isotope ratios and water content. Geochim Cosmochim Acta 200:280–294

Harte B, Cayzer N (2007) Decompression and unmixing of crystals included in diamonds from the mantle transition zone. Phys Chem Miner 34:647–656

Hayman PC, Kopylova MG, Kaminsky FV (2005) Lower mantle diamonds from Rio Soriso (Juina area, Mato Grosso, Brazil). Contrib Mineral Petrol 149:430–445

Hosoya T, Kubo T, Ohatani E, Sano A, Funakoshi K (2005) Water controls the fields of metastable olivine in cold subducting slabs. Geophys Res Lett. https://doi.org/10.1029/2005GL023398

Hu J, Sharp TG (2017) Back-transformation of high-pressure minerals in shocked chondrites: low-pressure mineral evidence for strong shock. Geochim Cosmochim Acta 215:277–294

Kawazoe T, Nishihara Y, Ohuchi T, Miyajima N, Maruyama G, Higo Y, Funakoshi K, Irifune T (2016) Creep strength of ringwoodite measured at pressure–temperature conditions of the lower part of mantle transition zone using a deformation–DIA apparatus. Earth Planet Sci Lett 454:10–19
Kimura M, Chen M, Yoshida Y, El Goresy A, Ohtani E (2004) Back-transformation of high-pressure phases in a shock melt vein of an H-chondrite during atmospheric passage: implications for the survival of high-pressure phases after decompression. Earth Planet Sci Lett 217:141–150
Knittle E, Jeanloz R (1987) The activation energy of the back transformation of silicate perovskite to enstatite. In: Manghnani M, Syono Y (eds) High pressure in mineral physics. Terra Scientific and American Geophysical Union, Washington, DC, pp 243–250
Kojitani H, Akaogi M (1994) Calorimetric study of olivine solid solutions in the system $Mg_2SiO_4$–$Fe_2SiO_4$. Phys Chem Miner 20:536–540
Kojitani H, Terata S, Ohsawa M, Mori D, Inaguma Y, Akaogi M (2017) Experimental and thermodynamic investigations on the stability of $Mg_{14}Si_5O_{24}$ anhydrous phase B with relevance to $Mg_2SiO_4$ forsterite, wadsleyite, and ringwoodite. Am Min 102:2032–2044
Kubo T, Kaneshima S, Torii Y, Yoshioka S (2009) Seismological and experimental constraints on metastable phase transformations and rheology of the Mariana slab. Earth Planet Sci Lett 287:12–23
Kubo T, Kimura M, Kato T, Nishi M, Tominaga A, Kikegawa T, Funakoshi K (2010) Plagioclase breakdown as an indicator for shock conditions of meteorites. Nat Geosci 3:41–45
Kubo T, Kato T, Higo Y, Funakoshi K-i (2015) Curious kinetic behavior in silica polymorphs solves seifertite puzzle in shocked meteorite. Sci Adv 1:1500075
Kubo T, Kono M, Imamura M, Kato T, Uehara S, Kondo T, Higo Y, Tange Y, Kikegawa T (2017) Formation of a metastable hollandite phase from amorphous plagioclase: a possible origin of lingunite in shocked chondritic meteorites. Phys Earth Planet Inter 272:50–57
Miyahara M, El Goresy A, Ohtani E, Nagase T, Nishijima M, Vashaei Z, Ferroir T, Gillet P, Dubrovinsky L, Simionovici A (2008) Evidence for fractional crystallization of wadsleyite and ringwoodite from olivine melts in chondrules entrained in shock-melt veins. Proc Natl Acad Sci U S A 105:8542–8547
Miyahara M, Ohtani E, Kimura M, El Goresy A, Ozawa S, Nagase T, Nishijima M, Hiraga K (2010) Coherent and subsequent incoherent ringwoodite growth in olivine of shocked L6 chondrites. Earth Planet Sci Lett 295:321–327
Miyahara M, Ohtani E, Ozawa S, Kimura M, El Goresy A, Sakai T, Nagase T, Hiraga K, Hirao N, Ohishi Y (2011) Natural dissociation of olivine to (Mg, Fe) $SiO_3$ perovskite and magnesiowustite in a shocked Martian meteorite. Proc Natl Acad Sci U S A 108:5999–6003
Miyahara M, Ohtani E, Nishijima M, El Goresy A (2019) Olivine melting at high pressure condition in the chassignite Northwest Africa 2737. Phys Earth Planet Inter 291:1–11
Moore RO, Gurney JJ (1985) Pyroxene solid solution in garnets included in diamond. Nature 318:553–555
Morishima H, Kato T, Suto M, Ohtani E, Urakawa S, Utsumi W, Shimomura O, Kikegawa T (1994) The phase boundary between α- and β-$Mg_2SiO_4$ determined by in situ X-ray observation. Science 265:1202–1203
Nishi M, Kubo T, Kato T, Tominaga A, Shimojuku A, Doi N, Funakoshi K, Higo Y (2010) Survival of majoritic garnet in diamond by direct kimberlite ascent from deep mantle. Geophys Res Lett. https://doi.org/10.1029/2010GL042706
Nishihara Y, Takahashi E, Matsukage KN, Iguchi T, Nakayama K, Funakoshi K (2004) Thermal equation of state of $(Mg_{0.91}Fe_{0.09})_2SiO_4$ ringwoodite. Phys Earth Planet Inter 143(144):33–46
Nishihara Y, Shinmei T, Karato S (2006) Grain-growth kinetics in wadsleyite: effects of chemical environment. Phys Earth Planet Inter 154:30–43
Nishiyama N, Wang Y, Sanehira T, Irifune T, Rivers ML (2008) Development of the multi-anvil assembly 6–6 for DIA and D-DIA type high-pressure apparatuses. High Press Res 28:307–314
Ohtani E, Kimura Y, Kimura M, Takata T, Kondo T, Kubo T (2004) Formation of high-pressure minerals in shocked L6 chondrite Yamato 791384: constraints on shock conditions and parent body size. Earth Planet Sci Lett 227:505–515
Paterson MS (1982) The determination of hydroxyl by infrared absorption in quartz, silicate glasses and similar materials. Bull Mineral 105:20–29
Pearson DG, Brenker FE, Nestola F, McNeill J, Nasdala L, Hutchison MT, Matveev S, Mather K, Silversmit G, Schmitz S, Vekemans B, Vincze L (2014) Hydrous mantle transition zone indicated by ringwoodite included within diamond. Nature 507:221–224
Reynard B, Takir F, Guyot F, Gwanmesia G, Liebermann R, Gillet P (1996) High-temperature Raman spectroscopic and X-ray diffraction study of beta-$Mg_2SiO_4$: insights into its high-temperature thermodynamic properties and the beta- to alpha-phase-transformation mechanism and kinetics. Am Min 81:585–594
Ringwood AE, Kesson SE, Hibberson W, Ware N (1992) Origin of kimberlites and related magmas. Earth Planet Sci Lett 113:521–538
Rubie DC, Ross CR (1994) Kinetics of olivine-spinel transformation in subducting lithosphere: experimental constrains and implications for deep slab processes. Phys Earth Planet Inter 86:223–241
Rubie DC, Tsuchida Y, Yagi T, Utsumi W, Kikegawa T, Shimomura O, Brearley AJ (1990) An in situ X ray diffraction study of the kinetics of the $Ni_2SiO_4$ olivine-spinel transformation. J Geophys Res 95:15829–15844
Sharp TG, Lingemann CM, Dupas C, Stöffler D (1997) Natural occurrence of $MgSiO_3$-ilmenite and evidence for $MgSiO_3$-perovskite in a shocked L chondrite. Science 277:352–355
Tappert R, Stachel T, Harris JW, Muehlenbachs K, Ludwig T, Brey GP (2005) Subducting oceanic crust: the source of deep diamonds. Geology 33:565–568
Tomioka N, Fujino K (1997) Natural (Mg, Fe)$SiO_3$-ilmenite and -perovskite in the Tenham meteorite. Science 277:1084–1086
Tomioka N, Miyahara M (2017) High-pressure minerals in shocked meteorites. Meteorit Planet Sci 52:2017–2039
Tomioka N, Mori H, Fujino K (2000) Shock-induced transition of $NaAlSi_3O_8$ feldspar into a hollandite structure in a L6 chondrite. Geophys Res Lett 27:3997–4000
Tschauner O, Ma C, Beckett JR, Prescher C, Prakapenka VB, Rossman GR (2014) Mineralogy. Discovery of bridgmanite, the most abundant mineral in Earth, in a shocked meteorite. Science 346:1100–1102
Tschauner O, Huang S, Yang S, Humayun M, Liu W, Stephanie Gilbert Corder SN, Bechtel HA, Tischler J, Rossman GR (2021) $CaSiO_3$-perovskite, as a mineral from the lower mantle. Science 374:891–894
Turnbull D (1956) Phase changes. In: Seitz F, Turnbull D (eds) Solid state physics, vol 3. Elsevier, Amsterdam, pp 225–306
Walton EL (2013) Shock metamorphism of Elephant Moraine A79001: implications for olivine–ringwoodite transformation and the complex thermal history of heavily shocked Martian meteorites. Geochim Cosmochim Acta 107:299–315
Wang Y, Guyot F, Liebermann RC (1992) Electron Microscopy of (Mg, Fe)$SiO_3$ perovskite: Evidence for structural phase transitions and implications for the lower mantle. J Geophys Res 97:12327–12347
Xie Z, Sharp TG (2007) Host rock solid-state transformation in a shock-induced melt vein of Tenham L6 chondrite. Earth Planet Sci Lett 254:433–445

## Publisher's Note